

SiO Molecular Jets around young stars - A numerical perspective

B. Vaidya^{1*}, Tom Douglas¹, Paola Caselli¹, Tom Hartquist¹

¹*School of Physics and Astronomy, University of Leeds, Leeds LS2 9JT*

29 July 2013

ABSTRACT

Key words: MHD – methods:numerical – ISM: jets and outflows

1 INTRODUCTION

Jets are one of the first manifestations of star formation in dense molecular cores. They are ubiquitous in both massive and low star forming regions. These supersonic flows perpendicular to the underlying accretion disk plays a vital role in removing excess angular momentum and thereby aiding in the accretion. For low mass stars, they are believed to be launched by magneto-centrifugally forces and further collimated by magnetic hoop stress (Blandford & Payne 1982; Konigl & Pudritz 2000). However, in case of high mass stars, radiative forces also contribute to flow dynamics during the later evolutionary stages Vaidya et al. (2011). Typically, these jets are few parsec size long and can be divided into three length-scale domains viz. source and disk scales ($1\text{--}10^2$ AU), envelope scales ($10^2\text{--}10^5$ AU) and parent cloud scales ($10^5\text{--}10^6$ AU) REFERENCE. Among them, the envelope scales are the ones where rich chemical evolution occurs as the jet interacts with the molecular medium. In this region, the jet propagates into a relatively static medium inducing shocks that are interesting from the physical and chemical point of view. In addition to shocks, molecular material from the surrounding is entrained and accelerated to high velocities giving rise to molecular outflows.

Bipolar molecular outflows from low and high mass stars have been studied in details over the past decade (see reviews by Bachiller 1996; Arce et al. 2007; Tafalla & Bachiller 2011). Advancement in millimeter interferometers have allowed to observe these outflows with high spatial resolution of few arc seconds. A large number of studies related to young outflows are done using standard outflow and shock tracer like CO and SiO respectively. In addition to these molecular tracers, shocks from these outflows are detected in molecular hydrogen using infra-red telescopes. Based on these observational studies, various empirical properties for these outflows have been discovered. For example, the CO

outflows from single dish studies are seen to be highly collimated for both low and high mass stars (for e.g., Gueth & Guilloteau 1999; Beuther et al. 2002) they are referred to as *molecular jets*. These outflows also exhibit a mass-velocity relation with a power law form $dM(v)/dv \propto v^{-\gamma}$, where values of γ range from 1 to 3 Downes & Cabrit (2003). Episodic knots believed to be caused by variable accretion events are a common property of young molecular outflows (for e.g. in L1577: Gueth et al. 1998, in HH300: Arce & Goodman 2001a). These knots show their signatures as *wedges* in the position-velocity (PV) diagrams Arce & Goodman (2001b). Also, most commonly observed in these outflows are signatures of rotation and precession (for e.g., in DG Tau: Bacciotti et al. 2002).

Even with myriad of empirical evidences, the exact nature of SiO and CO outflow is not clear. For a complete understanding it is imperative to compliment these observations with theoretical models. Many models based on hydro-simulations and steady state shock calculations were proposed to explain the observational signatures of molecular outflows. Among them the two main models are that of wide-angled wind driven Shu et al. (1991) and jet driven outflow Canto & Raga (1991). The most popular among them is the jet driven model as wind driven molecular outflows not only fail to match observed PV digrams Cabrit & Bertout (1992) but also tend to sweep large quantity of material at the extermities of the lobes Masson & Chernin (1992). While the jet driven models could successfully derive the global outflow shapes and mass velocity relations of CO outflows (Raga & Cabrit 1993; Masson & Chernin 1993) . There have also been some attempts to combine these two models into one Shang et al. (2006) to explain the global observational features. However, most of these dynamical models do not account for shock chemistry. Instead, shock chemistry is studied independently without dynamics using plane parallel shock models (Schilke et al. 1997; Flower et al. 2003) . The magneto-hydrodynamic (MHD) calculations by Glassgold et al. (1991) suggested that molecules like SiO and CO could as form within the jet. Similar conclusions of

* E-mail: B.Vaidya@leeds.ac.uk (BV)

molecules surviving in steady state disk winds have also been shown [Panoglou et al. \(2012\)](#). Very limited simulations have modelled the outflow dynamics including molecular chemistry but in absence of magnetic fields ([Raga et al. 1995](#); [Smith & Rosen 2003](#)).

In the present work, our goal is to take a step further in modelling of jet driven molecular outflows. The present model aims to consistently derive observed emission properties of molecular outflows, specifically various SiO line transitions, by combining axisymmetric MHD simulations of radiative jet propagation. In particular, we evolve the jet dynamical quantities in conjunction with different non-equilibrium cooling prescriptions of varying complexities. The most complex is that of molecular cooling along with H₂ chemistry. This prescription allows us to track the formation and destruction of HI, HII and H₂ along with the flow dynamics. The final state of the jet obtained for each cooling model is then post-processed using a non-LTE radiative line transfer code to obtain emission maps, spectra and PV diagram. These emission maps are further processed using ALMA-CASA pipeline to obtain synthetic images of molecular outflows.

In the next three sections we describe our numerical setup, cooling prescriptions and radiative transfer line code respectively. In Sect. 5, we will present results from the parameter survey and the discussions along with predicted ALMA maps will be presented in Section 6 and 7, followed by conclusions.

2 NUMERICAL SETUP

2.1 Numerical code and Equations

For our study, we carry out axisymmetric numerical ideal MHD simulations using the PLUTO code ([Mignone et al. 2007](#)) which is based on a conservative scheme of Godunov type. We have modified the original code to incorporate molecular cooling from self-consistent evolution of hydrogen chemistry (see Sect. 3).

In general, the MHD code considers the following set of equations. The conservation of the mass and the momentum,

$$\frac{\partial \rho}{\partial t} + (\vec{v} \cdot \nabla) \rho + \rho \nabla \cdot \vec{v} = 0 \quad (1)$$

$$\rho \left(\frac{\partial \vec{v}}{\partial t} + (\vec{v} \cdot \nabla) \vec{v} \right) = -\nabla P + \frac{1}{4\pi} (\nabla \times \vec{B}) \times \vec{B} \quad (2)$$

where ρ is gas density, \vec{v} the velocity vector, P the gas pressure, and \vec{B} the magnetic field vector with the poloidal and toroidal components - \vec{B}_p, B_ϕ . Note that the forces due to gravity are neglected for this problem as the domain of interest is far away from the central object (i.e., star).

The cooling function Λ which depends on temperature T , mass density ρ and chemical abundances \mathbf{X} , appears in the energy equation as a source term,

$$\frac{\partial}{\partial t} (\rho E) + \nabla \cdot \left[\rho E \vec{v} + \left(P + \frac{B^2}{8\pi} \right) \vec{v} \right] - \vec{B}(\vec{v} \cdot \vec{B}) = \Lambda(\rho, T, \mathbf{X}), \quad (3)$$

where the total energy density of the flow E comprises contributions from the internal energy ϵ , the mechanical energy

and the magnetic energy,

$$E = \epsilon + \frac{v^2}{2} + \frac{B^2}{8\pi\rho}. \quad (4)$$

The gas pressure in the flow is related to the density assuming an equation of state with the adiabatic index γ ,

$$P = (\gamma - 1)\rho\epsilon. \quad (5)$$

The evolution of chemical abundances for each species is solved via,

$$\frac{\partial \rho \mathbf{X}_i}{\partial t} + \nabla \cdot (\rho \mathbf{X}_i \vec{v}) = \rho \mathbf{S}_i, \quad (6)$$

where \mathbf{S}_i represents the net creation or destruction of a given species through chemical reactions (see Sect. 3).

The evolution of the magnetic field is governed by induction equation,

$$\frac{\partial \vec{B}}{\partial t} = \nabla \times (\vec{v} \times \vec{B}). \quad (7)$$

In addition to the above set of equations the code obeys the condition of divergence-free magnetic fields, $\nabla \cdot \vec{B} = 0$, which is numerically achieved by construction since using the Powell's eight wave formulation.

2.2 Initial Condition

We model the propagation of jet as it interacts with the molecular cloud core much further from the central object, i.e., > 1000 AU. Further away from the central source, the downward pull of gravity plays a negligible role and the dynamics of jet is primarily governed by magnetic fields. The total magnetic field in jet is dominated by the toroidal component. This is because the poloidal field decays as z^{-2} as compared to z^{-1} for toroidal field to maintain the force balance (z is the vertical distance from source). The hoop stress due to pinch force from toroidal magnetic fields maintains the a highly collimated beam like structure for the jet.

The ambient medium with which the jet interacts primarily represents the molecular cloud core. The numerical domain is axis-symmetric and in (r, z, ϕ) cylindrical coordinates. Its extent in radial direction is $20 R_j$ and $100 R_j$ along the vertical axis, R_j being the radius of the jet. The domain is resolved by a uniform grid with 200 cells in radial and 1000 cells in vertical direction. For simplicity, we choose this medium to be unmagnetized and non-turbulent. The density in the ambient medium varies with vertical height z as, $\rho_{\text{amb}} \sim (\rho_0/z^2)$ consistent with observations ([Caselli 2011](#)). The value of ρ_0 depends upon the density contrast, η , between the jet and the ambient medium. The number density in the jet is kept fixed such that the density in ambient medium lies within a range of $10^4 - 10^5 \text{ cm}^{-3}$. The pressure in the ambient molecular medium is set so to maintain a constant temperature of 50 K.

The jet enters into the medium through a nozzle of radius R_{jet} from the lower boundary ($z = 0$). The jet density is fixed to be 10^5 cm^{-3} and it has a radius of $2.5 \times 10^{15} \text{ cm} \sim 167$ AU. The jet is injected into the domain with a typical velocity of $v_{\text{jet},0} = 100 \text{ km/s}$ as is the case for most low mass stellar jets specially the low velocity component. The constant jet velocity is superimposed with periodic pulsation of the form,

$$v_{\text{jet}} = v_{\text{jet},0} (1.0 + A \sin(2.0\pi t/T_p)) \quad (8)$$

where the amplitude A is 0.25 and time period $T_p = 70$ years. The pressure at the surface of the jet is $10^{-10} \text{ dyne cm}^{-2}$ corresponding to a temperature of $T_{\text{jet}} \sim 4 \times 10^3 \text{ K}$. Inside the jet beam, a radial variation of thermal and magnetic pressure is adopted to maintain a magneto-static equilibrium. We adopt the same radial profiles used by [Stone & Hardee \(2000\)](#) for all our runs. Based on these profiles, the toroidal magnetic field is assumed to be zero at the axis and achieves a maximum at some radius, r_m inside the jet. The maximum value, $B_{\phi,m}$, depends on the plasma β which is a parameter used for our study along with the density contrast η .

In order to consistently model the SiO emission arising from shocks as this jet interacts with the medium, we evolve the dynamics along with chemistry and cooling prescriptions. They are described in details in the next section.

3 CHEMISTRY AND COOLING

3.1 Power law cooling

3.2 Atomic Cooling

3.3 Tabulated Cooling

3.4 Molecular Cooling

The evolution of molecular, atomic and ionized hydrogen is governed by equations listed in Table 1. In this cooling mode, these equations are evolved at each times using temperature dependent rates mentioned in the table along with their source. The code tracks the formation and destruction of three quantities viz., $X(\text{HI})$, $X(\text{H}_2)$ and $X(\text{HII})$ with a constraint that sum of all three should be unity. Further, these abundances are used to update the cooling function $\Lambda(n, T, \mathbf{X})$ to consistently derive the temperature for next advection step.

4 RADIATIVE TRANSFER

Radiative transfer modeling used for post processing.

4.1 The radiative transfer code

The radiative transfer program used is LIME (Line Modeling Engine; [Brinch & Hogerheijde 2010](#)), which calculates line intensities based on a weighted sample of randomly chosen points in a continuous 3D model. The method of selecting these points is given in section 4.2. At each of these points, the density of the main collision partner (equivalent amount of H_2 , given by $n(\text{H}_2) + 0.5 n(\text{H})$), gas and dust temperatures, velocity, molecular abundances and unresolved turbulent velocity are specified. These points are then smoothed by Lloyd's algorithm ([Lloyd 1982](#)) in order to minimise the variation in distance between points whilst keeping the same underlying distribution. These points are then connected by Delaunay triangulation and it is between the points connected by this method that photon are allowed to propagate (fig. 14). The level populations of the selected molecules are calculated at each of these points from collisional and radiative (de)excitation and the local radiation

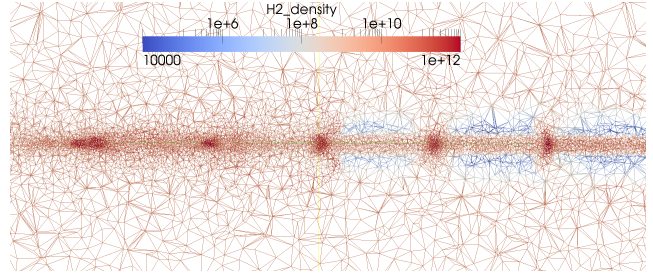


Figure 2. A plot of the points selected by the gridding process and the paths down which photons can propagate for points in the r, z plane. The points are color coded by the density distribution (in m^{-3} , as used in LIME) and are more concentrated in the high density knots.

field is calculated. This is repeated 20 times with the populations of each level converging towards a single value. This number of iterations is sufficient for the signal to noise ratio of the level populations (as defined in [Brinch & Hogerheijde 2010](#)) to exceed 1000 for 99% of the points, ensuring that the simulation has converged on a stable level population. After 20 iterations the model is ray-traced in order to produce synthetic brightness maps. The average of ten separate runs was taken to minimise the artefacts in the output images, resulting from the grid construction (Fig. 3).

4.2 Grid construction

In order to construct the grid, candidate points are randomly selected from the volume to be simulated. These candidates then have their equivalent H_2 number density, and the number density of SiO, compared against those of a reference point in order to decide if the candidate point is to be used in the grid or not. Candidate grid points are selected at random in a cylindrical coordinates that is linearly spaced in z and θ and logarithmically spaced in r . For each point to be selected, a random number α is drawn from the semi-open set $[0, 1)$ as a threshold. After selection of random coordinates, the H_2 density and SiO density at the candidate point (n and m , respectively) are compared against the densities of a reference point in the unperturbed ambient medium multiplied by $\frac{4\eta}{5}$ (n_0 and m_0). If $\alpha < \left(\frac{n}{n_0}\right)^{0.3}$ or $\alpha < \left(\frac{m}{m_0}\right)^{0.3}$ then the point is selected for use. Otherwise another r, θ, z co-ordinate is selected and it becomes the candidate point. In addition to this method of selection, 5% of the points are linearly distributed in x, y and z with no bias with regards to density or abundance. This provides a minimum level of sampling for the large low density regions in the outer parts of the simulated volume. See fig. 3 for an example of the points distribution in r, z . The function comparing the candidate point to the reference point and the candidate point distribution were selected empirically to sample all scales while ensuring that the majority of points are located in the inner disc where the density is higher.

4.3 SiO abundance

Need refs for this!! The amount of SiO is determined by the local velocity and temperature. The fractional abundance is given by the equation:

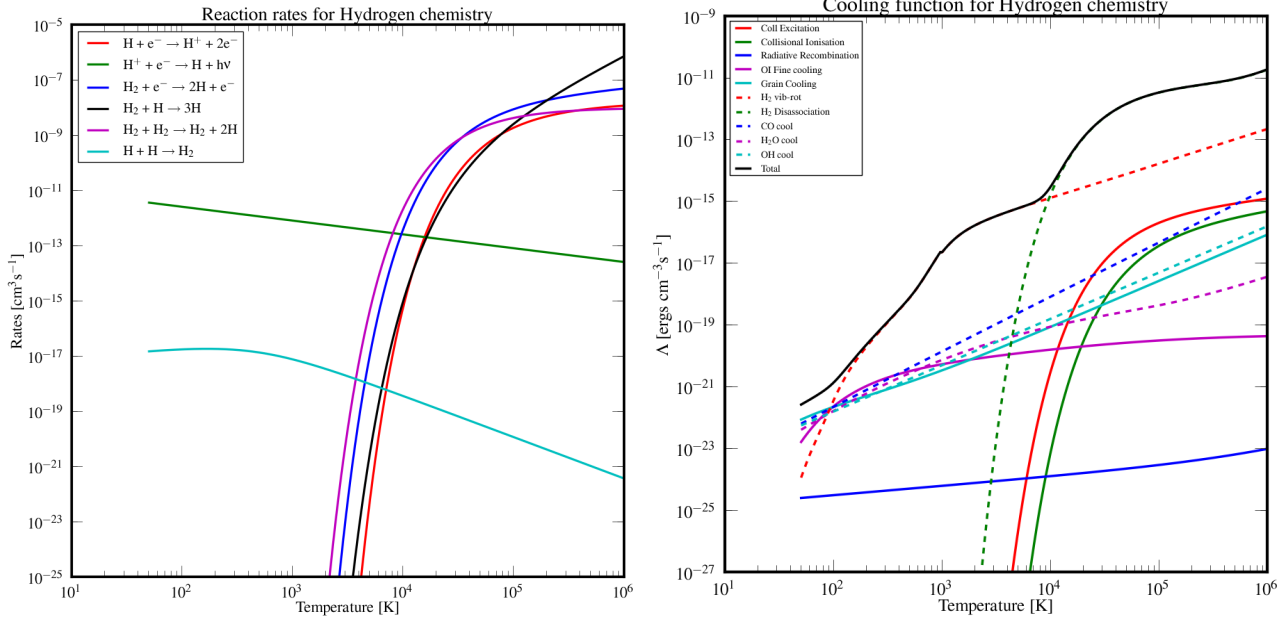


Figure 1. Variation of H_2 chemistry reaction rates, k_i and cooling function $\Lambda(n, T, \mathbf{X})$ with temperature for the initial state (see Sect. 3.4)

Table 1. Summary of the chemistry reaction set. T is the temperature in Kelvin, T_{eV} is the temperature in electron-volts, $T_5 = T/1 \times 10^5$ and $T_2 = T/100$

No.	Reaction	Rate Coefficient (cm^3s^{-1})	Reference ^a
1.	$\text{H} + \text{e}^- \rightarrow \text{H}^+ + 2\text{e}^-$	$k_1 = 5.85 \times 10^{-11} T^{0.5} \exp(-157,809.1/T)/(1.0 + T_5^{0.5})$	1
2.	$\text{H}^+ + \text{e}^- \rightarrow \text{H} + \text{h}\nu$	$k_2 = 3.5 \times 10^{-12} (T/300.0)^{-0.8}$	2
3.	$\text{H}_2 + \text{e}^- \rightarrow 2\text{H} + \text{e}^-$	$k_3 = 4.4 \times 10^{-10} T^{0.35} \exp(-102,000.0/T)$	3
4.	$\text{H}_2 + \text{H} \rightarrow 3\text{H}$	$k_4 = 1.067 \times 10^{-10} T_{\text{eV}}^{2.012} (\exp(4.463/T_{\text{eV}}))^{-1} ((1.0 + 0.2472 T_{\text{eV}})^{3.512})^{-1}$	4
5.	$\text{H}_2 + \text{H}_2 \rightarrow \text{H}_2 + 2\text{H}$	$k_5 = 1.0 \times 10^{-8} \exp(-84,100/T)$	2
6.	$\text{H} + \text{H} \xrightarrow{\text{dust}} \text{H}_2$	$k_6 = 3.0 \times 10^{-17} \sqrt{T_2} (1.0 + 0.4\sqrt{T_2} + 0.15 + 0.2T_2 + 0.8T_2^2)$	5

^a REFERENCES – (1) [Cen \(1992\)](#) [Eq. 26a]; (2) [Woodall et al. \(2007\)](#) [UMIST Database] (3) [Galli & Palla \(1998\)](#) [Eq. H17]; (4) [Abel et al. \(1997\)](#) [Tab. 3 Eq. 13]; (5) [Hollenbach & McKee \(1979\)](#) [Eq. 3.8]

$$\log(X) = -2.48 \times 10^{-8} v^5 + 5.50 \times 10^{-6} v^4 - 4.28 \times 10^{-4} v^3 + 1.24 \times 10^{-2} v^2 + 2.52 \times 10^{-2} v - 1.20 \times 10^1$$

where v is in kilometres per second. In addition to this if the temperature at the point is greater than 92,000K (the temperature of the Si-O bond disassociation energy) the abundance is reduced to 10^{-30} .

5 PARAMETER SURVEY

6 RESULTS

6.1 Comparison of cooling prescription

figure nos. 2 – Simulated images, emission maps for $\eta = 10$.

6.2 Molecular cooling and H_2 Chemistry

figure nos. 2 – Explain molecular cooling in more details. With the mechanism of formation and destruction of H , H_2 and H_2H using figures.

6.3 Effects of changing η and β

figure nos. 2 – Simulated images describing lengths, collimation and emission for lower η more stronger.

6.4 SiO Abundance profile

figure nos. 2 – Comparison of three profiles for SiO Abundance, Contour maps for two transitions for top hat profile.

6.5 Spectra and PV diagrams

figure nos. 1 – one transition 3 different angles, Comparison of spectra and line ratios

Table 2. Summary from parameter runs

Run	Cooling Mode	η	β	Peak Intensity [K]	FWHM at Bow Shock
adi1010	Nil (Adiabatic)	10	10		
pow1010	Power law	10	10		
atm1010	Atomic	10	10		
atm101	Atomic	10	1		
atm210	Atomic	2	10		
tab1010	Tabulated	10	10		
tab210	Tabulated	2	10		
mol1010	Molecular	10	10		
mol510	Molecular	5	10		

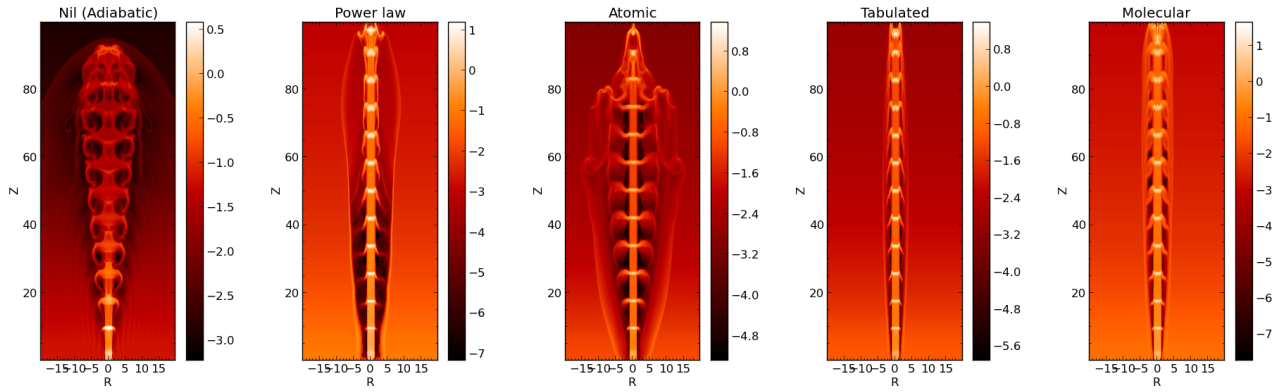


Figure 5. Jet Volume Density for different cooling modes with $\eta = 10$ and $\beta = 10$.

Table 1 – Parameter runs with changing β (magnetic fields) and η (density contrast) for cooling. Results should have Peak Intensity after convolution., FWHM at tip of bow shock.

Our reference run – $\beta = 10.0$, $\eta = 2.0$, with cooling and velocity dependent SiO Abundance.

Figure 3 – Output from MHD simulations (Reference run).

Figure 4 – Output from Rad Transfer (Reference run). Integrated Intensity Maps for different transitions for three different cooling prescriptions. (TODO : TOM)

Figure 5 – Spectra for the reference runs all transitions. (TODO : TOM)

Figure 6 – PV diagrams (TODO : TOM) for one transition in two directions. Figure 7 – Angle of Inclination dependence

emission. The low level transitions trace the region where the jet interacts with molecular medium. The clumpy nature in its emission is from the turbulent nature of its interaction. The higher transitions trace a much more collimated region along with the terminal shock. As seen by Chandler & Richer 2001 and Hirano 2006.

Advantage of non-LTE modeling over LVG Cabrit 2007, Lee 2008. Line ratios ~ 1 can be explained well.

EHV component ??

Limitations

7 DISCUSSION

Effects of varying η

Lower η gives better emission.

Importance of cooling prescriptions

Bulk of emission comes from cooling instabilities.

Effects of varying abundance profile ... Crucial ingredient in modeling molecular bullets

Spectra and PV Diagrams

Line - widths $\sim 15-25 \text{ km s}^{-1}$. Wedge shaped PV diagrams a signature feature of jet driven molecular outflows. Counterparts in observations.

Comparison with Observed results

Different line transition trace different components of SiO

8 ALMA VIEW

ALMA view of the reference run and stress of applying our synthetic techniques to study the molecular outflows in more details.

Figure 6. for ALMA –

9 CONCLUSION

We are the best in modelling SiO outflows.

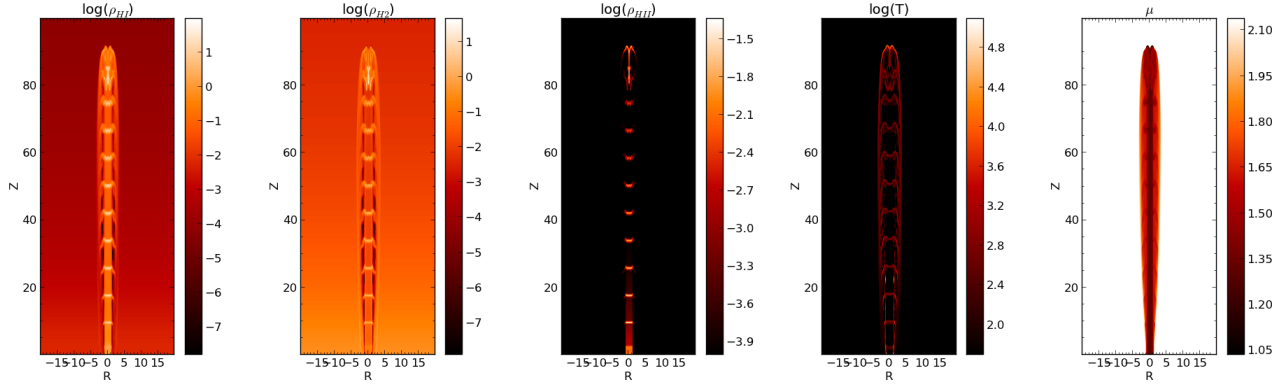


Figure 7. Fraction of hydrogen species in the run with molecular cooling having $\eta = 3$ and $\beta = 10$.

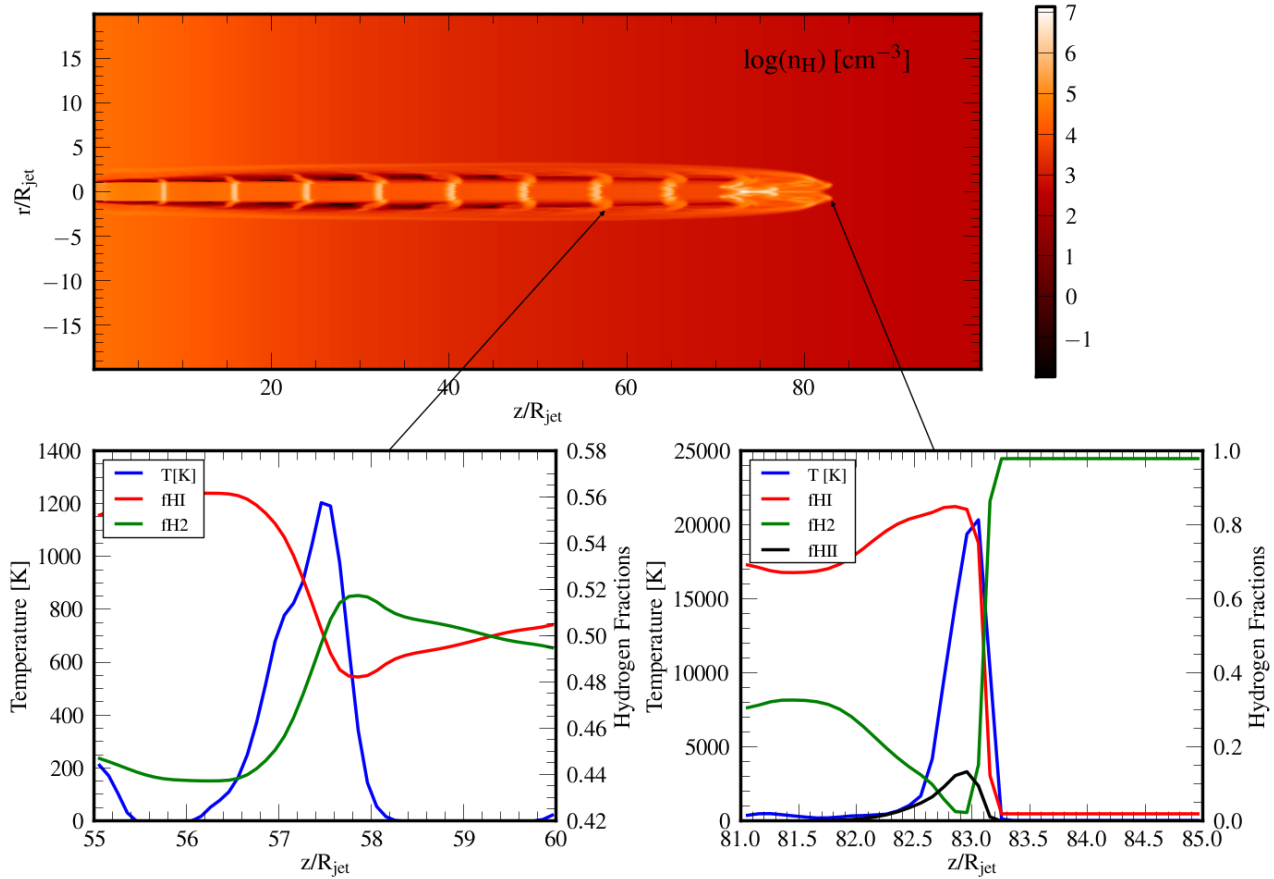


Figure 8. Dependence of hydrogen fractions on the temperature at two points in the flow, viz. the interface of the knot with molecular medium and at the bow shock

REFERENCES

- Abel T., Anninos P., Zhang Y., Norman M. L., 1997, *New A*, 2, 181
- Arce H. G., Goodman A. A., 2001a, *ApJ*, 554, 132
- Arce H. G., Goodman A. A., 2001b, *ApJ*, 551, L171
- Arce H. G., Shepherd D., Gueth F., Lee C.-F., Bachiller R., Rosen A., Beuther H., 2007, *Protostars and Planets V*, pp 245–260
- Bacciotti F., Ray T. P., Mundt R., Eisloffel J., Solf J., 2002, *ApJ*, 576, 222
- Bachiller R., 1996, *ARA&A*, 34, 111
- Beuther H., Schilke P., Gueth F., McCaughrean M., Andersen M., Sridharan T. K., Menten K. M., 2002, *A&A*, 387, 931
- Blandford R. D., Payne D. G., 1982, *MNRAS*, 199, 883
- Brinch C., Hogerheijde M. R., 2010, *A&A*, 523, A25
- Cabrit S., Bertout C., 1992, *A&A*, 261, 274
- Canto J., Raga A. C., 1991, *ApJ*, 372, 646
- Caselli P., 2011, in Cernicharo J., Bachiller R., eds, *IAU Symposium Vol. 280 of IAU Symposium, Observational*

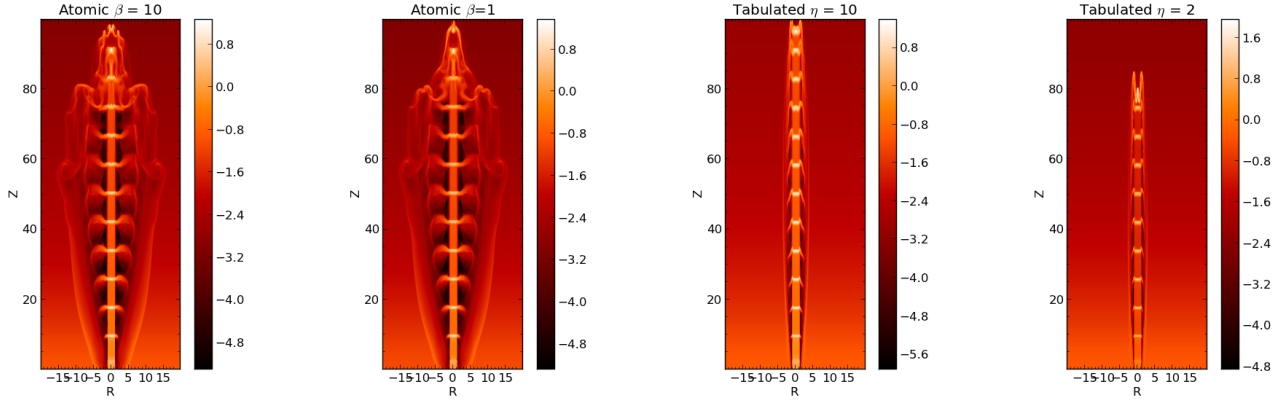


Figure 9. Jet Volume Density for atomic cooling with $\eta = 10$ but $\beta = 1$ and 10 and that with tabulated cooling with $\beta = 10$ but $\eta = 2$ and 10.

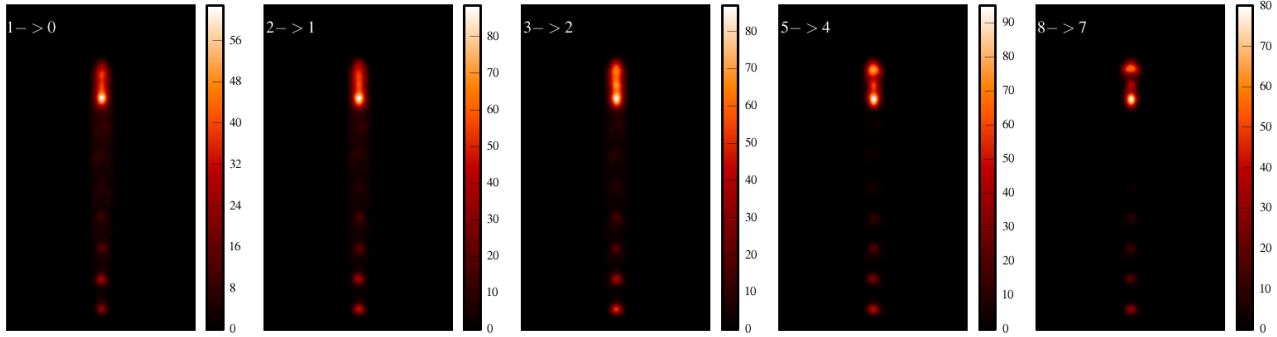


Figure 13. SiO emission from different line transitions for the run with molecular cooling having $\eta = 3$ and $\beta = 10$ using top-hat fractional abundance profile.

Studies of Pre-Stellar Cores and Infrared Dark Clouds. pp 19–32

Cen R., 1992, ApJS, 78, 341

Downes T. P., Cabrit S., 2003, A&A, 403, 135

Flower D. R., Le Bourlot J., Pineau des Forêts G., Cabrit S., 2003, MNRAS, 341, 70

Galli D., Palla F., 1998, A&A, 335, 403

Glassgold A. E., Mamon G. A., Huggins P. J., 1991, ApJ, 373, 254

Gueth F., Guilloteau S., 1999, A&A, 343, 571

Gueth F., Guilloteau S., Bachiller R., 1998, A&A, 333, 287

Hollenbach D., McKee C. F., 1979, ApJS, 41, 555

Konigl A., Pudritz R. E., 2000, Protostars and Planets IV, p. 759

Lloyd S., 1982, Information Theory, IEEE Transactions on, 28, 129

Masson C. R., Chernin L. M., 1992, ApJ, 387, L47

Masson C. R., Chernin L. M., 1993, ApJ, 414, 230

Mignone A., Bodo G., Massaglia S., Matsakos T., Tesileanu O., Zanni C., Ferrari A., 2007, ApJS, 170, 228

Panoglou D., Cabrit S., Pineau Des Forêts G., Garcia P. J. V., Ferreira J., Casse F., 2012, A&A, 538, A2

Raga A., Cabrit S., 1993, A&A, 278, 267

Raga A. C., Taylor S. D., Cabrit S., Biro S., 1995, A&A, 296, 833

Schilke P., Walmsley C. M., Pineau des Forêts G., Flower D. R., 1997, A&A, 321, 293

Shang H., Allen A., Li Z.-Y., Liu C.-F., Chou M.-Y., An-

derson J., 2006, ApJ, 649, 845

Shu F. H., Ruden S. P., Lada C. J., Lizano S., 1991, ApJ, 370, L31

Smith M. D., Rosen A., 2003, MNRAS, 339, 133

Stone J. M., Hardee P. E., 2000, ApJ, 540, 192

Tafalla M., Bachiller R., 2011, in Cernicharo J., Bachiller R., eds, IAU Symposium Vol. 280 of IAU Symposium, Molecules in Bipolar Outflows. pp 88–102

Vaidya B., Fendt C., Beuther H., Porth O., 2011, ApJ, 742, 56

Woodall J., Agúndez M., Markwick-Kemper A. J., Millar T. J., 2007, A&A, 466, 1197

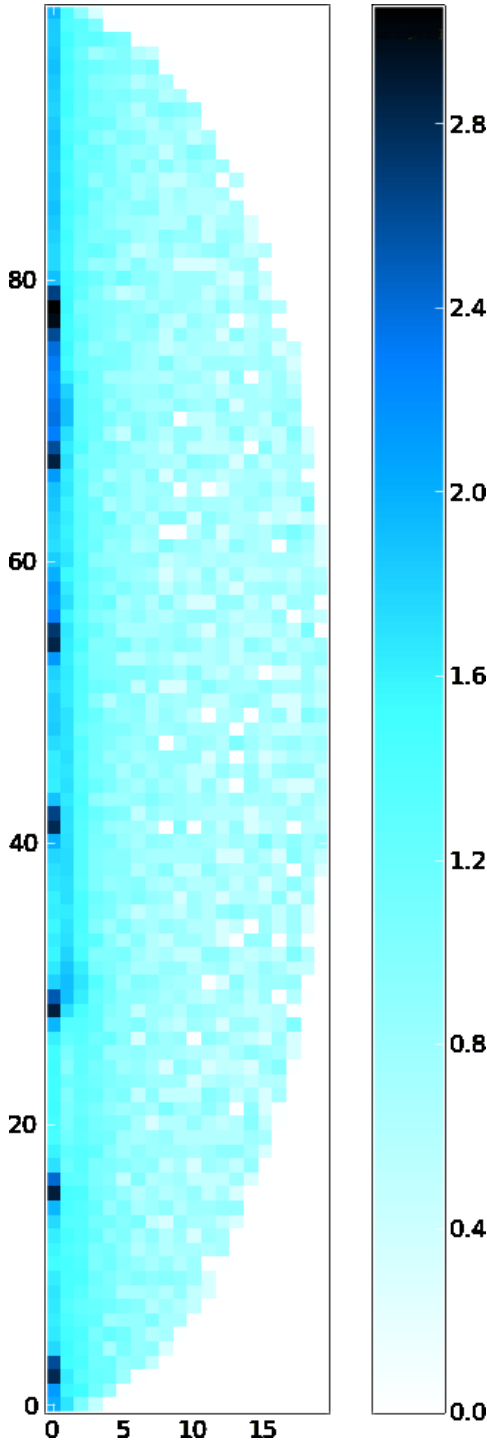


Figure 3. A 2D histogram of the point distribution throughout the model. The disc and envelope can be seen as two separate entities which have to be sampled using different point distributions.

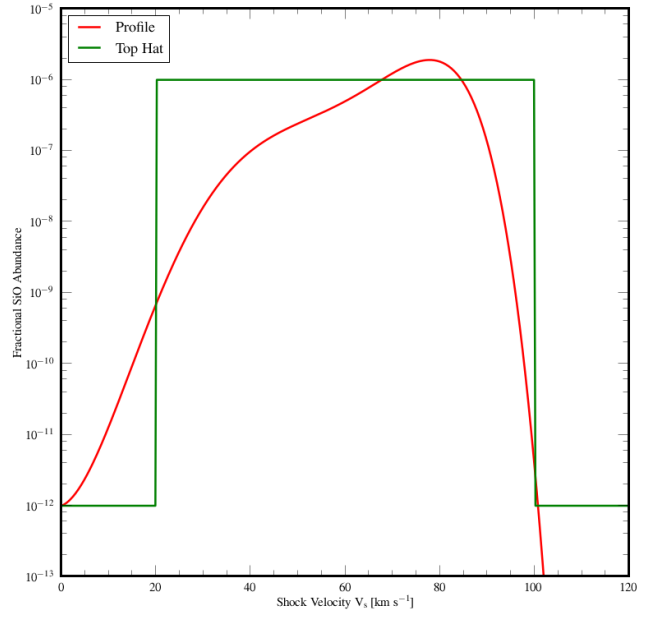


Figure 4. The different fractional SiO abundances as a function of shock velocity, V_s .

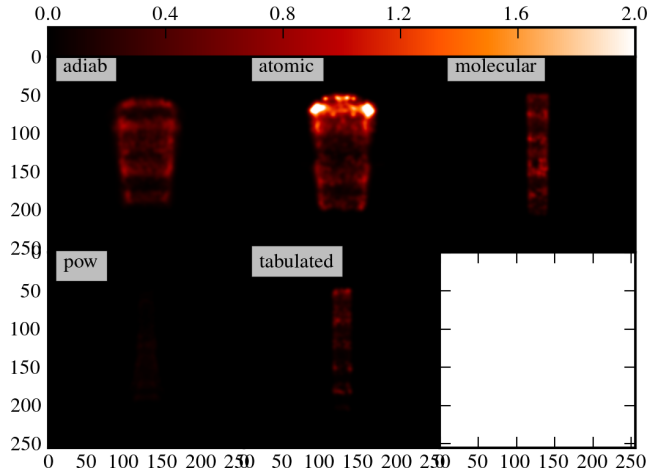


Figure 6. A plot of the integrated SiO J2-1 emission from 5 models, each using a different method to calculate cooling and all with $\eta=10$ $\beta=10$.

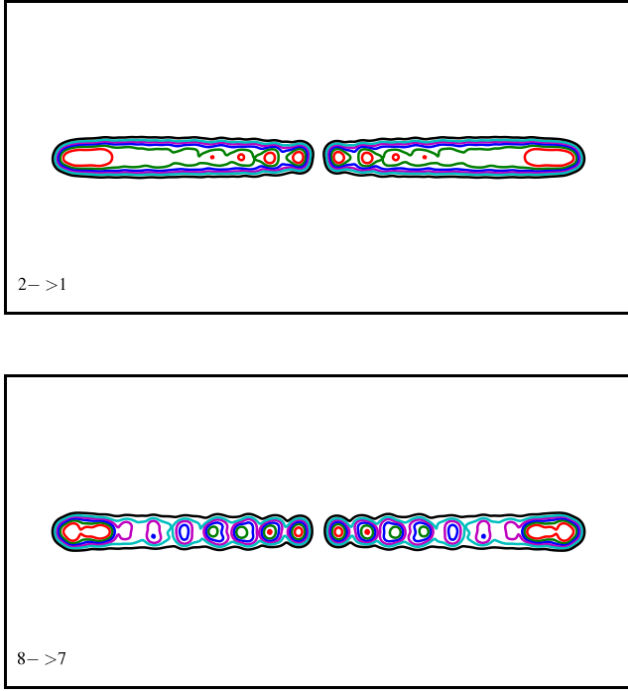


Figure 10. Contours of SiO 2->1 and 8->7 emission obtained using the SiO Top Hat profile.

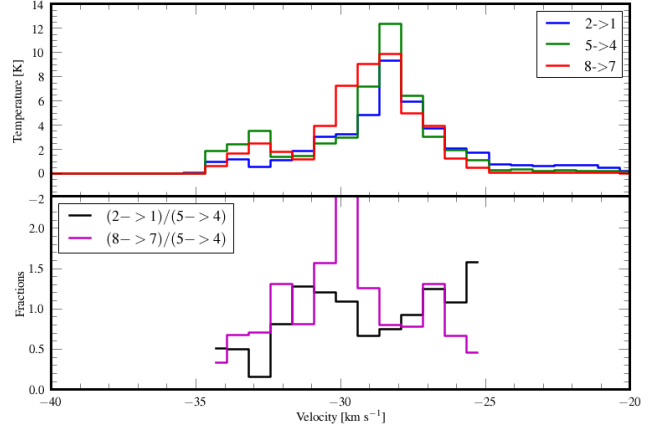


Figure 14. *Top* Line profiles in SiO J = 2-1, 5-4 and 8-7 at one the inner knot for the molecular cooling run with $\eta = 3$ and $\beta = 10$ using top hat abundance profile. The profiles are obtained when the angle of inclination is 60° with respect to line of sight. *Bottom* Line temperature ratios $T(8-7)/T(5-4)$ and $T(2-1)/T(5-4)$, as a function of velocity

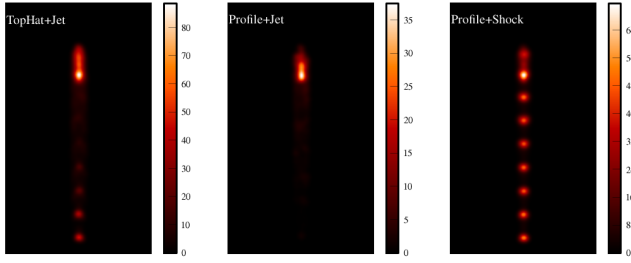


Figure 11. Variation of 2->1 SiO emission for runs with molecular cooling having $\eta = 3$ and $\beta = 10$ and different abundance profiles.

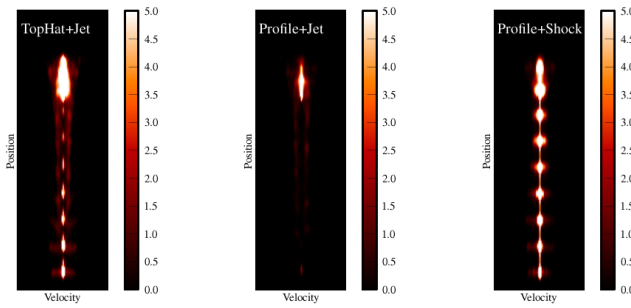


Figure 12. Variation of position-velocity diagram for 2->1 SiO emission for runs with molecular cooling having $\eta = 3$ and $\beta = 10$ and different abundance profiles.